

1 **Azimuthal dependence of GNSS-R scattering**  
2 **cross-section in hurricanes**

3 **Rajeswari Balasubramaniam, Christopher Ruf**

4 University of Michigan, Ann Arbor

5 **Key Points:**

- 6 • Azimuthal variations of GNSS-R scattering cross-section in hurricanes are mod-  
7 eled with sinusoidal harmonics.  
8 • The azimuthal harmonics explain 2-8% of the overall variation in scattering cross-  
9 section.  
10 • The magnitude of the azimuthal harmonics increases with increasing wind speed.

This is the author manuscript accepted for publication and has undergone full peer review but has not been through the copyediting, typesetting, pagination and proofreading process, which may lead to differences between this version and the [Version of Record](#). Please cite this article as doi: [10.1029/2020JC016167](https://doi.org/10.1029/2020JC016167)

---

Corresponding author: Rajeswari Balasubramaniam, [rajibala@umich.edu](mailto:rajibala@umich.edu)

This article is protected by copyright. All rights reserved.

## Abstract

GNSS-R measurements of the ocean surface are sensitive to roughness scales ranging from a few cms to several kms. Inside a hurricane the surface roughness changes drastically due to varying sea age and fetch length conditions and complex wave-wave interactions caused by its cyclonic rotation and translational motion. As a result, the relationship between the surface roughness at different scale sizes becomes azimuthally dependent, as does the relationship between scattering cross section and wind speed as represented by a Geophysical Model Function (GMF). In this work, the impact of this azimuthal variation on the scattering cross-section is assessed. An empirical GMF is constructed using measurements by the NASA CYclone Global Navigation Satellite System (CYGNSS) matched to HWRF reanalysis surface winds for 19 hurricanes in 2017 and 2018. The analysis reveals a 2-8 % variation in scattering cross-section due to azimuthal location and the magnitude of the azimuthal dependence is found to grow with wind speed.

## Plain Language Summary

GNSS-Reflectometry (GNSS-R) is a technique of studying reflected GPS signals to extract useful information about the surface. CYGNSS is the first of its kind GNSS-R constellation mission selected by NASA's earth venture program. The goal of the mission is to understand inner core processes in hurricanes by making accurate surface wind speed measurements there. Wind speed at the surface is determined using a GMF that maps the reflection measurement to a wind speed. Due to the complex nature of sea state and wave interactions inside a hurricane, measured scattering cross-section depends on the azimuthal location of the measurement inside the hurricane system. A modified GMF is proposed here that accounts for the azimuthal dependence. The model is developed by matching up CYGNSS measurements to hurricane winds estimated by the NOAA HWRF model for 19 hurricanes during 2017 and 2018. The new GMF accounts for a 2-8 % variation in the measurements due to azimuthal location which increases with wind speed.

## 1 Introduction

The measurement of hurricane wind fields has a long history, ranging from airborne measurements (Jones et al., 1981; Wright et al., 2001; Uhlhorn et al., 2007) to space borne observations made by microwave radiometers and radars (Ebuchi et al., 2002; Figa-Saldaña et al., 2002; Gaiser et al., 2004). The key challenges for mapping the complex hurricane wind fields are the need for adequate spatial and temporal sampling of such fast evolving phenomena and the ability to penetrate through strong rain bands to measure the surface winds. Global Navigation Satellite System Reflectometry (GNSS-R) is a relatively new field of remote sensing that uses the existing GNSS signals to study the surface. It greatly improves the sampling and revisit capability by utilizing the existing GPS transmitter constellation and its L-band measurements are less affected by the heavy precipitation in the rain bands.

A GNSS-R system is a bistatic radar in a specular forward scattering geometry. A number of airborne (Garrison et al., 1998; Katzberg et al., 2001; Garrison et al., 2002) and spaceborne GNSS-R systems (Gleason, 2013; Foti et al., 2015; Soisuvarn et al., 2016) have verified the ability of this configuration to successfully retrieve ocean surface winds from space. A GNSS-R radar measures the scattering cross-section of the surface around the region of specular reflection. The reflected GPS signal observed by a GNSS-R receiver is mapped into delay-doppler space for different time delays and doppler shifts observed. This forms the Delay-Doppler Map (DDM) of the surface (Gleason et al., 2009).

It is important to note that the scattering cross section measured by a GNSS-R receiver is directly related to the surface roughness rather than the surface wind itself. GNSS-R forward scatter is quasi specular incoherent scatter in most conditions. Thus an appropriate Mean Squared Slope (MSS) of the surface as sensed by GNSS-R mea-

61 surements is an integration of the wave spectrum over a range of wavelengths ranging  
62 from several meters up to a few tens of cms. The surface MSS is inversely related to the  
63 measured normalised bistatic radar cross section ( $\sigma_0$ ). The Geophysical Model Function  
64 (GMF) maps this  $\sigma_0$  to the ocean surface wind speed empirically to retrieve the near sur-  
65 face wind speed from the measurements. In a hurricane environment, with complex tem-  
66 poral and spatial distribution of wind and wave fields, it is a challenging task to accu-  
67 rately retrieve wind speed from GNSS-R measurements. The scattering cross-section de-  
68 pends on surface roughness scales spanning a wide range from small capillary waves to  
69 long gravity waves. In fully developed seas, with essentially infinite sea age and fetch length,  
70 the relative magnitude of the surface roughness at different scale sizes reaches an equi-  
71 librium state due to energy cascade and dissipation mechanisms. Inside a hurricane, how-  
72 ever, the sea age and fetch length conditions can vary significantly with azimuthal lo-  
73 cation due to its rotational and translational motion. This can perturb the balance be-  
74 tween the roughness at different scales and alter the measured scattering cross section.  
75 Despite its complex nature, several simulations (Moon et al., 2003; Fan et al., 2009; Young,  
76 2017), directional buoy measurements (Young, 2006) and airborne missions (Walsh et  
77 al., 1985; Wright et al., 2001; Uhlhorn et al., 2007) have, over the years, helped develop  
78 directional wave spectra for hurricanes. The directional wave spectra acquired from sev-  
79 eral hurricane reconnaissance missions suggest that local wind and wave directions vary  
80 sinusoidally with the azimuth angle referenced to the hurricane heading and have a weak  
81 radial dependence (Hwang et al., 2017). These results suggest that remote sensing tech-  
82 niques such as GNSS-R, which depend on surface wave scattering, should consider az-  
83 imuthal wind-wave response functions for accurate modeling and subsequent wind re-  
84 trieval.

85 A GNSS-R Geophysical Model Function describes the relationship between mea-  
86 sured scattering cross section and the 10m reference wind speed. Previous empirical GMFs  
87 for hurricane winds have been developed without allowing for possible dependence on  
88 azimuthal location within the storm (Clarizia et al., 2014; Ruf & Balasubramaniam, 2018).  
89 As a result, actual azimuthal dependencies are essentially averaged out and wind speed  
90 retrieval errors will be correlated with azimuth location. An improved, azimuthally de-  
91 pendent, empirical GMF is developed here to better account for the azimuthal variation  
92 of the wind and wave directions. A large dataset of observations from the CYGNSS mis-  
93 sion is used. CYGNSS is a NASA mission that was launched in Dec 2016. It has 8 mi-  
94 cro satellites equally spaced around a 520 km circular orbit inclined at 35 degrees. Each  
95 satellite carries a GNSS-R radar receivers tuned to measure GPS L1 signals at 1.575 GHz,  
96 thereby enabling it to make measurements through heavy precipitation regions with a  
97 mean revisit time of 7 hrs. The DDM measurements are made at a rate of 1 Hz and have  
98 continued uninterrupted since March 2017.

99 In this work, the impact of azimuthal variation on the measured scattering cross-  
100 section is assessed using CYGNSS data over 19 major hurricanes across different basins  
101 during 2017 and 2018. For this analysis, HWRP reanalysis hurricane winds are used as  
102 a reference. The remainder of this paper is structured as follows. Section 2 gives a de-  
103 scription of the datasets used and the observations from the CYGNSS-HWRP matchup  
104 analysis. Section 3 describes the empirical GMF developed as a function of azimuth an-  
105 gle; Section 4 assesses the performance of the proposed model and Section 5 provides the  
106 conclusions of the study.

## 107 2 Theory and Observations

108 For this analysis, the v2.1 release of CYGNSS Level 1  $\sigma_0$  measurements over 19 ma-  
109 jor hurricanes from 2017 and 2018 are used (PO.DAAC, 2018). The data are matched  
110 to Hurricane Weather Research and Forecasting (HWRP) reanalysis winds of the inner  
111 nest grid spacing of 2 km. The HWRP winds are re-sampled to CYGNSS resolution and  
112 are empirically paired to CYGNSS  $\sigma_0$  observations with a maximum temporal separa-  
113 tion of 60 minutes and a maximum spatial separation of 0.25 deg lat and lon. The matchups

| West Pacific | East Pacific | Atlantic | Indian |
|--------------|--------------|----------|--------|
| Jebi         | Aletta       | Florence | Mekunu |
| Jelawat      | Otis         | Harvey   | Titli  |
| Mangkhut     | Willa        | Irma     |        |
| Maria        |              | Jose     |        |
| Trami        |              | Maria    |        |
| Walaka       |              | Michael  |        |
| Yutu         |              | Oscar    |        |

**Table 1.** Hurricanes from different basins in the CYGNSS-HWRF matchup dataset.

114 are then translated into a storm-centric-direction of motion based coordinate system for  
 115 the purpose of understanding the azimuthal variation of measurements relative to the  
 116 storm heading. The Weather Research and Forecast (WRF) system for hurricane pre-  
 117 diction (HWRF) is an operational model developed by the National Centers for Envi-  
 118 ronmental Prediction (NCEP). HWRF provides 3 domains (one parent and 2 nested)  
 119 and is based on the initial position of the storm and on the National Hurricane Center  
 120 (NHC) forecast of the 72 hour storm position. The 2 nested domains move along the storm  
 121 with a coverage of 24 deg x 24 deg and 7 deg x 7 deg for the middle and the inner nest  
 122 respectively (Tallapragada et al., 2014). For our purposes, we use the inner nest grid-  
 123 ding that offers the finest resolution of about 0.015 deg (approx. 2kms). The CYGNSS  
 124 level 1  $\sigma_0$  are also filtered by several quality measures for this analysis. Only observa-  
 125 tions with high antenna gain ( $> 5dB$ ) and the overall quality flag set to best quality are  
 126 used. This has allowed a total dataset consisting of  $\sim 187,000$  observations in hurricanes  
 127 by CYGNSS. Table.1 lists the different hurricanes contained in this dataset.

128 The CYGNSS wind retrieval algorithm uses the two measured observables namely,  
 129 the normalized bistatic radar scattering cross section ( $\sigma_0$ ) and the slope of the leading  
 130 edge of the radar return pulse scattered by the ocean surface (LES) (Clarizia & Ruf, 2016).  
 131 With these observables, GMFs are empirically derived by pairing near co-incident inde-  
 132 pendent estimates of 10 meter referenced ocean surface wind. For a fully developed sea  
 133 (FDS), which constitutes the majority of the measurements, the observables are matched  
 134 to the ground truth reference which is the combination of European Centre for Medium-  
 135 Range Weather Forecasts (ECMWF) and Global Data Assimilation System (GDAS) re-  
 136 analysis wind speed products. This results in a FDS GMF. For young sea conditions with  
 137 limited fetch (YSLF), as observed in hurricanes, a YSLF GMF is generated using matchups  
 138 with near co-incident NOAA P-3 hurricane hunter passes over the major Atlantic storms  
 139 in 2017 (Ruf & Balasubramaniam, 2018). Examples of the FDS and YSLF GMFs are  
 140 shown in Fig.1 for observations at incidence angles of 10, 30 and 50 deg. Above wind speeds  
 141 of  $\sim 15m/s$ , the two GMFs diverge due to the underdeveloped state of seas near trop-  
 142 ical cyclones, which tends to lower the roughness and increase the scattering cross sec-  
 143 tion. One important feature to note is the difference in the slope of the two GMFs at  
 144 higher wind speeds. The YSLF GMF at high wind speeds has a higher value and a shal-  
 145 lower slope (lower  $|d\sigma_0/du_{10}|$ ) for all incidence angles. In general, the high wind slope  
 146 of the GMF can be used as a proxy for sea state development, with lower magnitudes  
 147 being associated with younger seas.

148 Fig.2 shows the distribution of winds in different quadrants of a hurricane using  
 149 the CYGNSS-HWRF matchup dataset. The wind distribution inside the hurricane strongly  
 150 varies in the azimuthal sense. In theory, the first quadrant is the generation region (shown  
 151 in Fig.3 (a)) and has the maximum energy. Also, quadrant 1 has the largest wind speeds  
 152 relative to the surface because the winds generated by the storm in this region are added  
 153 to the storm motion. The wind generates a spectrum of waves with different group ve-

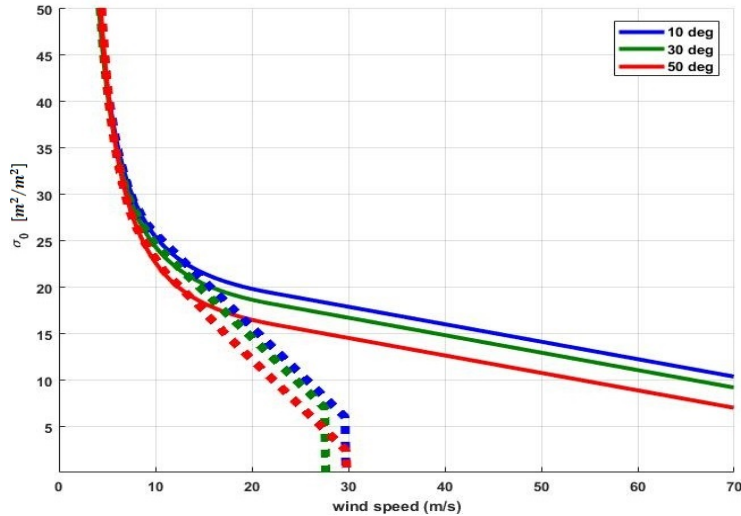


**Figure 1.** CYGNSS GMF for FDS winds shown by dotted lines and YSLF winds shown with solid lines. Incidence angles of 10, 30 and 50 deg are shown.

154 locities. Waves that have their group velocity equal to the velocity of the forward motion  
 155 of the storm remain in the intense wind region and receive maximum energy from  
 156 the wind. Waves with group velocity greater than storm forward motion velocity will out-  
 157 run the storm and propagate ahead as swell waves and those with a lower group veloc-  
 158 ity than the storm will be outrun by the storm and will be left behind (Young, 1999).  
 159 The swell radiating out ahead of the storm will often interact with the local calm sea in  
 160 phase quadrature, resulting in a confused sea condition. This is generally observed ahead  
 161 of the storm and to the rear of the storm, resulting in a younger sea in each of those re-  
 gions. The adequacy of a single slope for the GMF is assessed by determining the slope

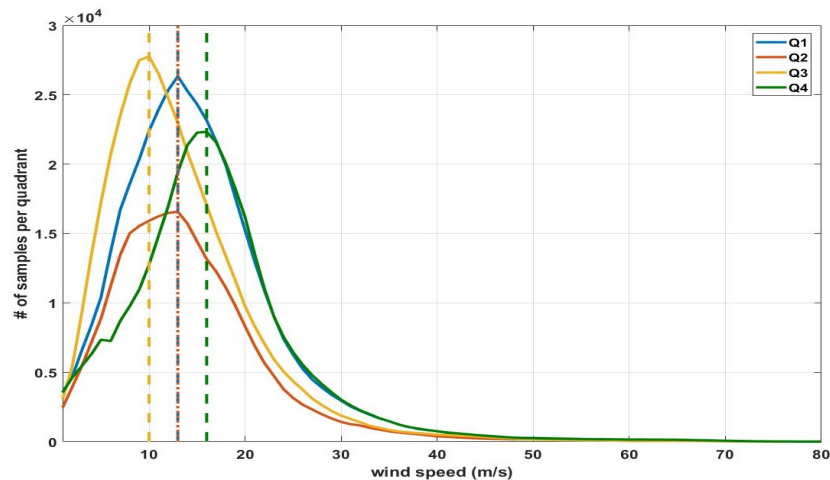


**Figure 2.** Distribution of winds in different quadrants in a storm relative to its heading.

162 separately in each quadrant of a storm, relative to the storm heading. The storm quad-  
 163 rants are defined based on the Cartesian representation of quadrants with increasing az-  
 164imuth angle in the anti-clockwise direction (see Fig.3 (a)). An example track of CYGNSS  
 165

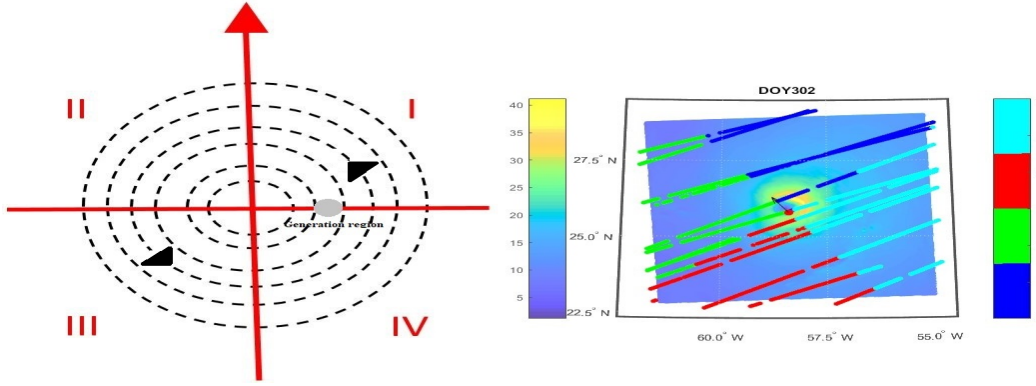


**Figure 3.** (a) Description of storm-centric-direction of motion based coordinate system used in this paper. (b) Sample CYGNSS tracks overlaid on HWRP wind field. HWRP wind intensity is shown by the colorbar on the left and the quadrant of the CYGNSS sample is shown by the colorbar on the right.

166 overlaid on HWRP, partitioned by storm quadrant (color bar on the right) is shown in  
 167 Fig.3 (b), the storm heading is represented by the black arrow at the storm center (iden-  
 168 tified by the red circle).

For the purpose of analysis, the range of HWRP wind speeds from 20 m/s to 70 m/s is divided into bins. The center of each wind speed bin is stepped in 1m/s increments from 20m/s to 70m/s. Within a bin, all corresponding CYGNSS scattering cross-section measurements are averaged together. The wind speeds are binned in this way to reduce biases in the estimation process due to variations in sample size at different wind speeds. The width of each wind speed bin is chosen based on the RMS difference plot shown in Fig.4 (a). RMS difference is evaluated by

$$RMSD(w_i) = \text{sqrt} \langle (\sigma_{0i} - \bar{\sigma}_{0i})^2 \rangle \quad (1)$$

169 Here  $\sigma_{0i}$  is the set of radar cross-section measurements in the  $i$ th wind bin,  $w_i$  and  $\bar{\sigma}_{0i}$   
 170 is the mean value of the cross-section in the given bin. The bin width is set as a vari-  
 171 able parameter and the error for different wind speed ranges and bin widths are plot-  
 172 ted in Fig.4 (a). The RMS difference is found to be roughly constant for bin widths up  
 173 to  $\pm 5$  m/s thus for optimal performance, we choose a width of  $\pm 4$  m/s for the  
 174 analysis throughout this paper. Fig.4 (b) shows the GMF for different storm quadrants.  
 175 The slope is derived by linear regression over the binned radar cross-section, as described  
 176 above. These GMFs at high winds can be seen to vary with quadrants. This is consis-  
 177 tent with the azimuthal variation of the local wind wave directions in published direc-  
 178 tional wavenumber spectrum datasets (B24, I09, I12 and I14) (Hwang et al., 2018). Quad-  
 179 rant 3 has the highest GMF, indicating a relatively younger sea condition. Quadrant 2  
 180 has the lowest GMF, indicating an extended fetch and duration, therefore a longer sea  
 181 age.

### 182 3 Harmonic Model Function

An empirical GMF is developed here which includes first and second order harmonic dependence on azimuthal location within the storm. This approach is based on the idea that any azimuthally varying function can be modelled as a linear combination of sinusoids. This technique is commonly used to represent the azimuthal dependence of radar and radiometer observations of ocean surface winds (Wentz & Smith, 1999; Meissner &



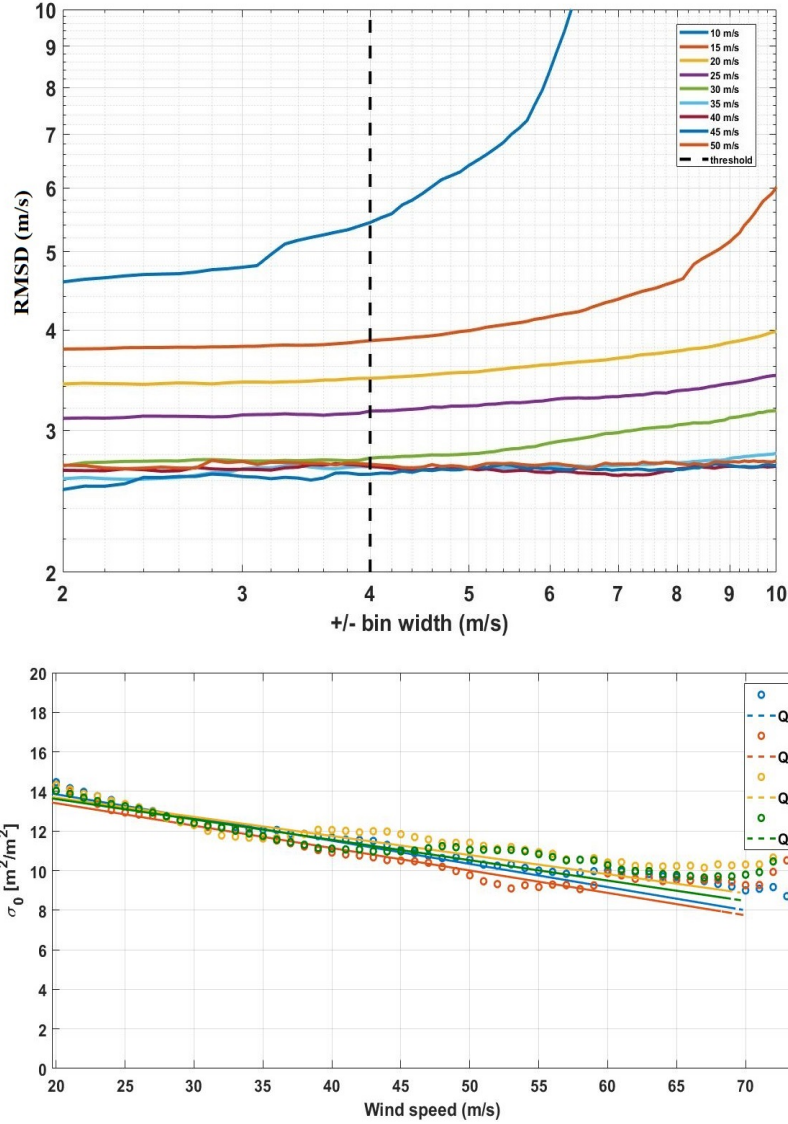


**Figure 4.** (a) Choice of wind speed averaging bin width based on RMS error. (b) GMF for different quadrants.

Wentz, 2002). The functional form of the model is given by

$$\sigma_0 = f(w, \phi) = a_0(w) + b_1(w)\sin(\phi) + b_2(w)\sin(2\phi) \quad (2)$$

183 where  $w$  is the wind speed,  $\phi$  is the azimuth angle, and  $(a_0, b_1, b_2)$  are model param-  
 184 eters that depend on wind speed. Note that the slope of the GMF above  $\sim 20\text{m/s}$  is the  
 185 same for different incidence angles. Apart from the wind speed dependence of  $\sigma_0$ , it also  
 186 has a dependence on incidence angle as shown in Fig.1. However, due to the limited size  
 187 of the sample population, the dependence on incidence and azimuth angles cannot be  
 188 separated. One way to address this issue is by maintaining a similar incidence angle dis-  
 189 tribution at all azimuth angles. This will mitigate the effect and the three parameter har-  
 190 monic model which results can be considered to represent the azimuthal dependence aver-  
 191 aged across all incidence angles. It should be noted that the strength of the azimuthal

dependence may vary with incidence angle. Additionally, note that if  $b_1 = b_2 = 0$ , the new GMF essentially defaults to the earlier azimuth-free version.

The  $\sigma_0$  observations are averaged over wind speed bins which are  $\pm 4m/s$  wide and the parametric model described above is fit to the observations for wind speed  $> 15m/s$  by nonlinear least squares minimization. The three model parameters ( $a_0, b_1, b_2$ ) are shown vs. wind speed in Fig.5 (a-c). The estimated parameters are shown in blue and the black-dashed lines represent the 95% confidence intervals on these estimates. Examples of the full GMF vs/ azimuth angle at 20, 40 and 60 m/s are shown in Fig.5 (d). Several important features of the GMF behavior can be observed. First, the magnitude of  $\sigma_0$  decreases with increasing wind speed, similar to the previous GMF behavior. Secondly, the azimuthal dependence of the GMF increases with increasing wind speed. Thirdly, the maximum value of  $\sigma_0$  occurs in the third quadrant for each wind speed, consistent with the GMF magnitude noted in Fig.4 (b). The minimum lies in the second quadrant thus, has a higher sea age and fetch conditions.

These effects are further illustrated in Fig.6, which plots the peak-to-peak azimuthal variation in  $\sigma_0$  vs. wind speed. The azimuthal variation rises steadily between  $\sim 30$  and  $55m/s$ . The drop-off in azimuthal variation above  $55m/s$  may be a result of the small number of samples available and the lower sensitivity to changes in wind speed.

#### 4 Performance Assessment

To assess the ability of the proposed model to capture the azimuthal variation in  $\sigma_0$ , several statistical measures of performance are considered. The robustness of the model is evaluated by breaking the total dataset into 3 subsets using every third element. The model is then trained on one subset and the relative RMSE is evaluated on another dataset. This relative error formulation is given by

$$RelativeError(\%) = \frac{\sqrt{\langle (\sigma_0 - \tilde{\sigma}_0)^2 \rangle}}{\langle \sigma_0 \rangle} * 100 \quad (3)$$

Here  $\sigma_0$  is the measurement sample at a given wind speed bin and  $\tilde{\sigma}_0$  is the model estimate of scattering cross-section for a given wind speed and azimuth information. Fig.7 (a) shows the behavior of relative error vs. wind speed for the different combinations of training and testing subsets. The dashed line represents use of the total dataset and hence is a test of internal consistency in the generation of the GMF. The large relative error at the lower wind speeds ( $< 15m/s$ ) is due to the fact that the model has been trained only for higher wind speeds.

The relative error is consistent over the 3 different datasets (D1, D2 and D3) as well as over the total dataset thus indicating the robustness of the developed model. Also, for wind speeds  $> 60m/s$  the relative error becomes noisy and this is attributed to the sparse observations at such high winds. Next, the dataset is divided into 2 independent subsets (D1 and D2) with storms well mixed from different basins and years and the analysis is repeated. The result is shown in Fig.7 (b). The relative error is consistent over a wide range of wind speeds from 20–60m/s re-attesting to the robustness of the model.

The next performance metric is a statistical measure of the percentage of azimuthal variation captured by the model over different wind speed ranges. The metric used for this purpose is given by

$$1 - \frac{\mathbf{var}(\tilde{\sigma}_0)}{\mathbf{var}(\sigma_0)} * 100 = \begin{cases} 1, & \text{if model captures azimuth information completely.} \\ 0, & \text{if model doesn't capture any azimuth information.} \end{cases} \quad (4)$$

Here  $\mathbf{var}(\cdot)$  refers to the variance of the sample population,  $\sigma_0$  is the measurements and  $\tilde{\sigma}_0$  the model. The assumption behind this statistical metric is that the total variance in the observations at a given wind speed is associated with multiple factors, one



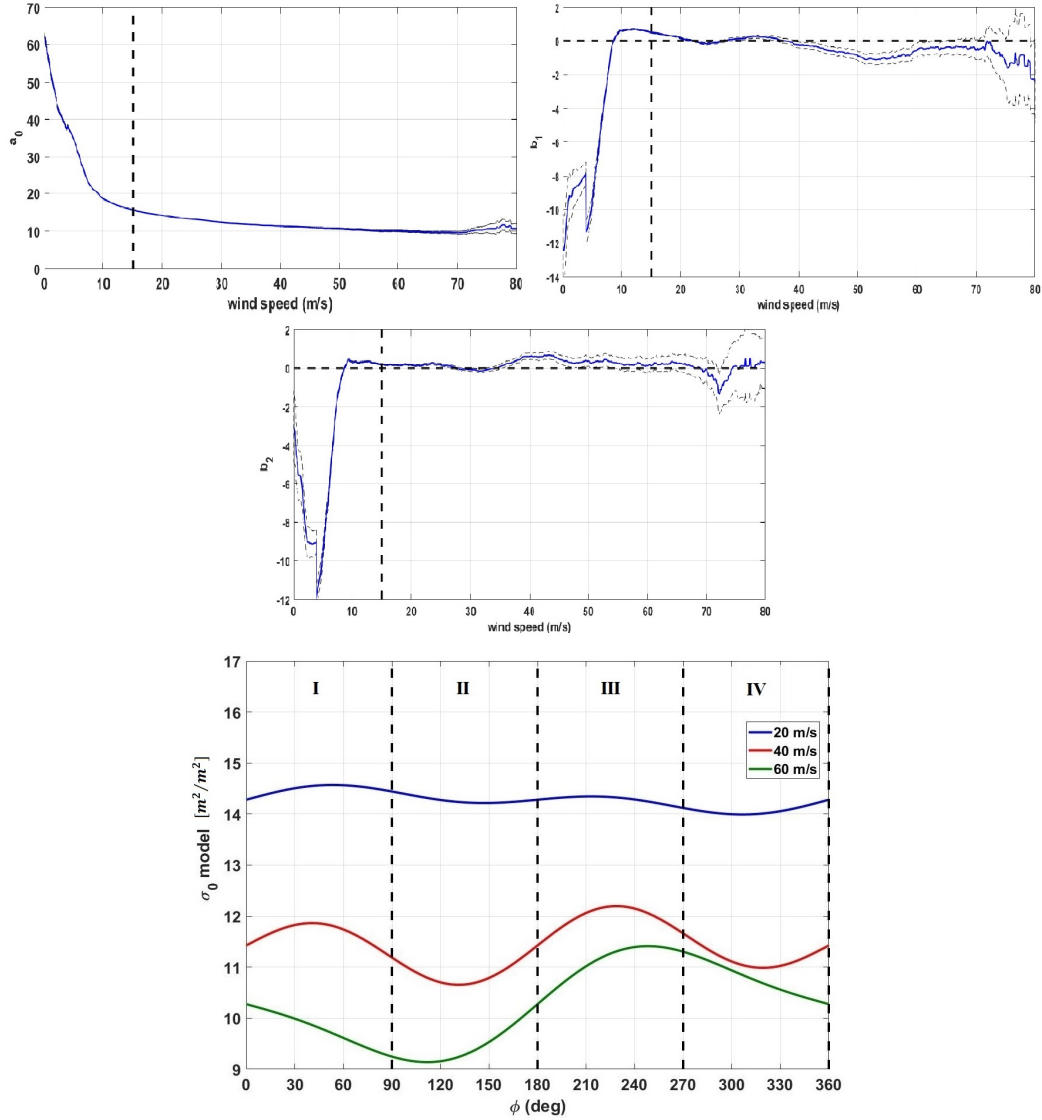


**Figure 5.** (a)-(c) Model parameters for azimuth GMF. (d) Azimuthal model for scattering cross-section shown for 3 different wind speeds.

233 of which is azimuthal variation. Since the model explicitly accounts for azimuthal vari-  
 234 ation, any residual variance in the model should be due to other factors than azimuthal  
 235 variation. If the metric is 1, it indicates that the model has captured all of the azimuth  
 236 information and, if the metric is 0, no azimuth information is captured. Fig.8 shows the  
 237 behavior of this metric tested for different wind speeds. The metric suggests that the model  
 238 is consistent and is able to capture greater than 90 % of the azimuthal variation over a  
 239 broad range of wind speeds between 20 and 60 m/s. Lower wind speeds are shown here  
 240 for completeness and again, at higher winds the performance drops due to sparse obser-  
 241 vations in the region.

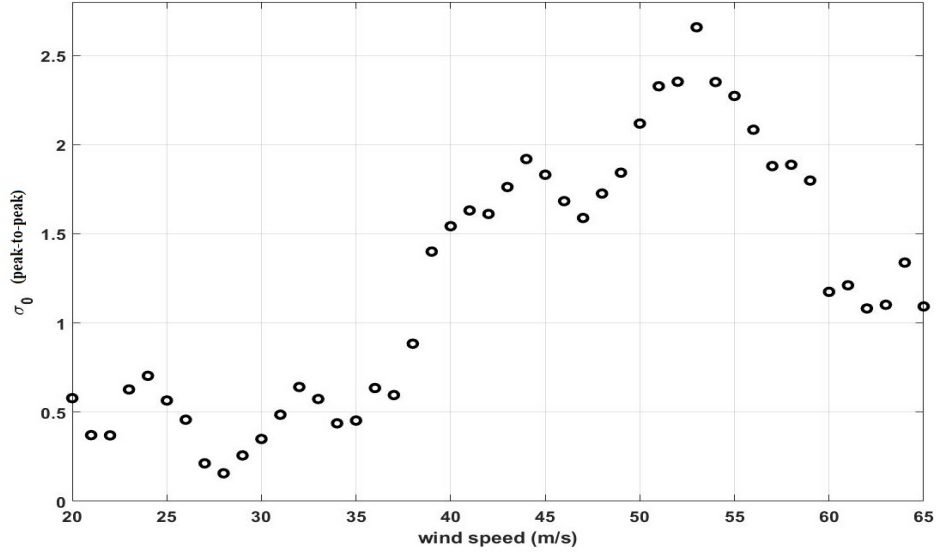


**Figure 6.** Peak-to-Peak azimuthal variation of scattering cross-section for different wind speeds.

Finally, we evaluate the total error in the observed scattering cross-section due to the azimuthal variation. The measure is defined by

$$Error(\%) = abs \left( 1 - \frac{MSD(\sigma_0, \tilde{\sigma}_0)}{\mathbf{var}(\sigma_0)} \right) * 100 \quad (5)$$

Here,  $MSD(\cdot)$  is the mean squared difference between the observations and the model estimate for a given wind speed and  $\mathbf{var}(\cdot)$  is the total variance in the observation for a given wind speed. If the MSE between the observation and the model is the same as the variance in the observation, it suggests that no azimuthal error is observed and if the MSE is negligible compared to the total variance in the observation, then most of the error in the  $\sigma_0$  can be associated to azimuthal variation. Fig.9 shows the % error in the scattering cross-section caused by the azimuthal variation. The model suggests a 2-8 % error in the scattering cross section for the wind speed range 20-60 m/s. The error is close to 2% at 20 m/s and gradually increases to 8 % around 53 m/s, then begins to reduce above that. While the overall error due to azimuthal variation is negligible, understanding the effect of this variation gives important insight into the wave properties inside a hurricane and its impending impact on the scattering cross-section. The increase in azimuthal variation with increase in wind speed also suggests that the GNSS-R scattering cross-section could be sensitive to the directional properties of wind at higher wind speed ranges.

## 5 Discussion and Conclusion

The specular bistatic scattering cross section of the ocean surface in tropical cyclones, as measured by GNSS-R radar receivers on the CYGNSS spacecraft, is found to depend on azimuthal location relative to the direction of storm motion. The dependence is caused by variations in the sea age and fetch length with storm quadrant, which affects the balance between surface roughness at short (capillary) and long (gravity) wavelengths. The roughness spectrum, in turn, affects the scattering cross section. A modified Geophysical Model Function (GMF) is developed using a second order harmonic expansion to represent the azimuthal dependence. The zeroth order term in the GMF

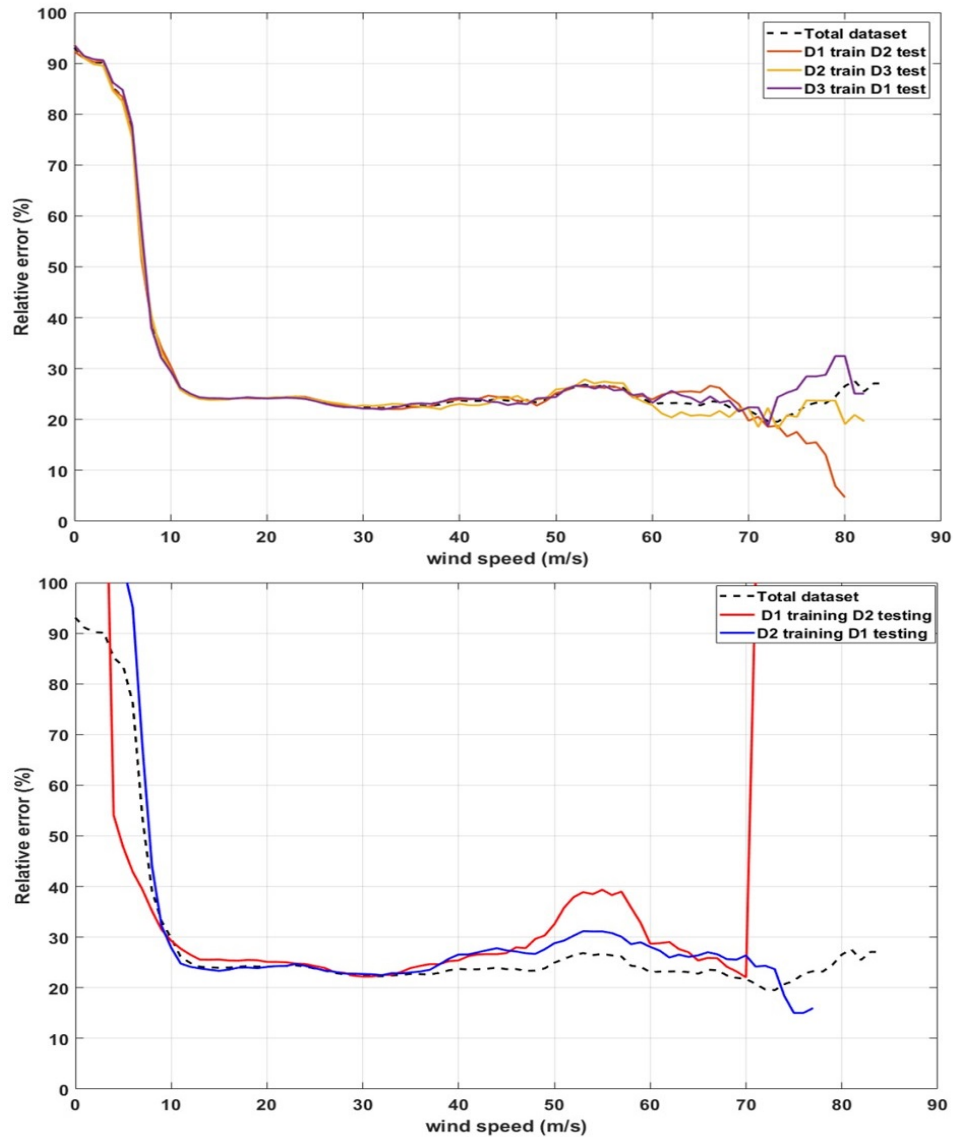


**Figure 7.** (a) RMSE for training and testing on 3 subsets (D1, D2 and D3). (b) RMSE for training and testing of 2 independent datasets (D1 and D2).

266 is consistent with previous models which have not included an azimuthal dependence.  
 267 The first and second order terms together explain between 2 and 8% of the total vari-  
 268 ance in the scattering cross section, with higher explained variance being associated with  
 269 higher wind speeds. The azimuthal corrections to the GMF are found to be significant  
 270 above  $\sim 20\text{m/s}$ . Above  $\sim 60\text{m/s}$ , the results are inconclusive owing to the scarcity of  
 271 samples.

272 It is worthwhile to note that the current GMF used by the CYGNSS project does  
 273 not include an azimuthal dependence in organized storms. Another difference from the  
 274 GMF developed here is the source of reference winds. The v2.1 GMF was developed using  
 275 matchups with near-surface wind measurements made by the Stepped Frequency Mi-  
 276 crowave Radiometer on NOAA hurricane hunter aircraft (Ruf & Balasubramaniam, 2018),  
 277 whereas the GMF developed here uses matchups with HWRP model winds. Differences  
 278 in overall magnitude between the two GMFs are likely a result of these differences.

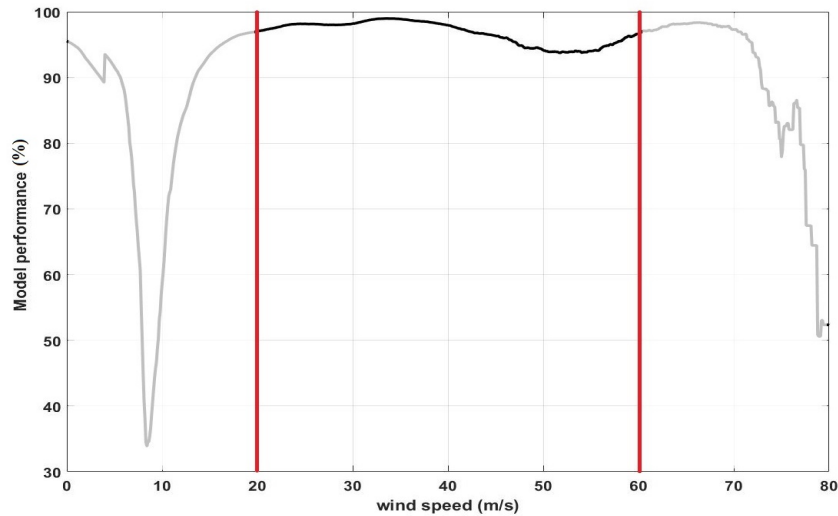


**Figure 8.** Evaluation of azimuthal information captured by the model.

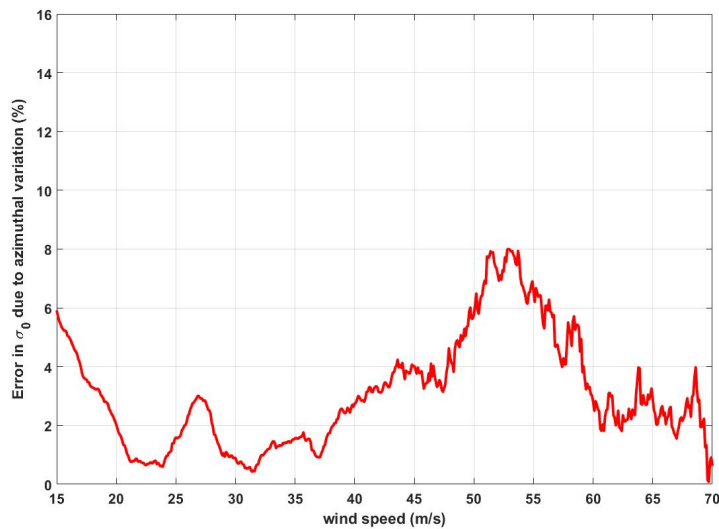


**Figure 9.** Error associated with scattering cross-section due to azimuthal variation.

279 The azimuthally dependent GMF has utility in two regards. It can serve as an indicator of sea state development in the inner core of tropical cyclones, for use in process  
 280 studies into air-sea and wind-wave interactions. It could also be used to improve wind speed retrieval algorithms in tropical cyclones that are based on GNSS-R observations.  
 281 Retrieval algorithms essentially invert the GMF to estimate wind speed given the scattering cross section, and a more physically representative forward GMF will allow for  
 282 a more accurate inversion. This type of study can also be extended to other non-TC weather systems with younger seas or scenarios with limited fetch conditions, e.g, limited fetch  
 283 on the lee side of major islands that may result in a different relationship between wind speed and MSS or  $\sigma_0$ , and therefore require a modified GMF for accurate wind speed  
 284 retrieval. The next steps in this work will be to implement the proposed azimuthal GMF for CYGNSS wind retrieval and evaluate its performance.  
 285  
 286  
 287  
 288  
 289

## Acknowledgments

The work presented was supported in part by NASA Science Mission Directorate contract NNL13AQ00C with the University of Michigan.

The Cyclone Global Navigation Satellite System (CYGNSS) Level 1 Science data record version 2.1 were obtained from the NASA EOSDIS Physical Oceanography Distributed Active Archive Center (PO.DAAC) at the Jet Propulsion Laboratory, Pasadena, CA (DOI: 10.5067/CYGNS-L1X21).

The HWRF reanalysis model data were obtained from the NOAA/NWS/NCEP/Environmental Modeling Center (<https://www.nco.ncep.noaa.gov/pmb/products/hur/>).

## References

- Clarizia, M. P., & Ruf, C. S. (2016). Wind speed retrieval algorithm for the cyclone global navigation satellite system (cygnss) mission. *IEEE Transactions on Geoscience and Remote Sensing*, *54*(8), 4419–4432.
- Clarizia, M. P., Ruf, C. S., Jales, P., & Gommenginger, C. (2014). Spaceborne gnss-r minimum variance wind speed estimator. *IEEE transactions on geoscience and remote sensing*, *52*(11), 6829–6843.
- Ebuchi, N., Graber, H. C., & Caruso, M. J. (2002). Evaluation of wind vectors observed by quikscat/seawinds using ocean buoy data. *Journal of Atmospheric and Oceanic Technology*, *19*(12), 2049–2062.
- Fan, Y., Ginis, I., Hara, T., Wright, C. W., & Walsh, E. J. (2009). Numerical simulations and observations of surface wave fields under an extreme tropical cyclone. *Journal of Physical Oceanography*, *39*(9), 2097–2116.
- Figa-Saldaña, J., Wilson, J. J., Attema, E., Gelsthorpe, R., Drinkwater, M. R., & Stoffelen, A. (2002). The advanced scatterometer (ascat) on the meteorological operational (metop) platform: A follow on for european wind scatterometers. *Canadian Journal of Remote Sensing*, *28*(3), 404–412.
- Foti, G., Gommenginger, C., Jales, P., Unwin, M., Shaw, A., Robertson, C., & Rosello, J. (2015). Spaceborne gnss reflectometry for ocean winds: First results from the uk techdemosat-1 mission. *Geophysical Research Letters*, *42*(13), 5435–5441.
- Gaiser, P. W., St Germain, K. M., Twarog, E. M., Poe, G. A., Purdy, W., Richardson, D., . . . others (2004). The windsat spaceborne polarimetric microwave radiometer: Sensor description and early orbit performance. *IEEE Transactions on Geoscience and Remote Sensing*, *42*(11), 2347–2361.
- Garrison, J. L., Katzberg, S. J., & Hill, M. I. (1998). Effect of sea roughness on bistatically scattered range coded signals from the global positioning system. *Geophysical research letters*, *25*(13), 2257–2260.
- Garrison, J. L., Komjathy, A., Zavorotny, V. U., & Katzberg, S. J. (2002). Wind speed measurement using forward scattered gps signals. *IEEE Transactions on Geoscience and Remote Sensing*, *40*(1), 50–65.
- Gleason, S. (2013). Space-based gnss scatterometry: Ocean wind sensing using an empirically calibrated model. *IEEE transactions on geoscience and remote sensing*, *51*(9), 4853–4863.
- Gleason, S., Gebre-Egziabher, D., & Egziabher, D. G. (2009). Gnss applications and methods.
- Hwang, P. A., Fan, Y., Ocampo-Torres, F. J., & García-Nava, H. (2017). Ocean surface wave spectra inside tropical cyclones. *Journal of Physical Oceanography*, *47*(10), 2393–2417.
- Hwang, P. A., Fan, Y., & Walsh, E. J. (2018). Hurricane hunter observations of wind and wave spectral properties: Implications on tropical cyclone remote sensing. In *Igarss 2018-2018 ieee international geoscience and remote sensing symposium* (pp. 149–152).
- Jones, W. L., Black, P. G., Delnore, V. E., & Swift, C. T. (1981). Airborne mi-

- 344           crowave remote-sensing measurements of hurricane allen. *Science*, *214*(4518),  
345           274–280.
- 346 Katzberg, S. J., Walker, R. A., Roles, J. H., Lynch, T., & Black, P. G. (2001). First  
347           gps signals reflected from the interior of a tropical storm: Preliminary results  
348           from hurricane michael. *Geophysical Research Letters*, *28*(10), 1981–1984.
- 349 Meissner, T., & Wentz, F. (2002). An updated analysis of the ocean surface wind  
350           direction signal in passive microwave brightness temperatures. *IEEE Transactions*  
351           *on Geoscience and Remote Sensing*, *40*(6), 1230–1240.
- 352 Moon, I.-J., Ginis, I., Hara, T., Tolman, H. L., Wright, C., & Walsh, E. J. (2003).  
353           Numerical simulation of sea surface directional wave spectra under hurricane  
354           wind forcing. *Journal of physical oceanography*, *33*(8), 1680–1706.
- 355 PO.DAAC, C. . (2018). Cygnss level 1 science data record version 2.1. ver.  
356           2.1. *PO.DAAC, CA, USA*. Retrieved from [https://doi.org/10.5067/](https://doi.org/10.5067/CYGNSS-L1X21)  
357           *CYGNSS-L1X21*
- 358 Ruf, C. S., & Balasubramaniam, R. (2018). Development of the cygnss geophysical  
359           model function for wind speed. *IEEE Journal of Selected Topics in Applied*  
360           *Earth Observations and Remote Sensing*, *12*(1), 66–77.
- 361 Soisuvarn, S., Jelenak, Z., Said, F., Chang, P. S., & Egido, A. (2016). The gnss  
362           reflectometry response to the ocean surface winds and waves. *IEEE Journal*  
363           *of Selected Topics in Applied Earth Observations and Remote Sensing*, *9*(10),  
364           4678–4699.
- 365 Tallapragada, V., Bernardet, L., Biswas, M. K., Gopalakrishnan, S., Kwon, Y., Liu,  
366           Q., . . . others (2014). Hurricane weather research and forecasting (hwrp)  
367           model: 2013 scientific documentation. *HWRF Development Testbed Center*  
368           *Tech. Rep*, *99*.
- 369 Uhlhorn, E. W., Black, P. G., Franklin, J. L., Goodberlet, M., Carswell, J., & Gold-  
370           stein, A. S. (2007). Hurricane surface wind measurements from an operational  
371           stepped frequency microwave radiometer. *Monthly Weather Review*, *135*(9),  
372           3070–3085.
- 373 Walsh, E., Hancock III, D., Hines, D., Swift, R., & Scott, J. (1985). Directional wave  
374           spectra measured with the surface contour radar. *Journal of physical oceanog-*  
375           *raphy*, *15*(5), 566–592.
- 376 Wentz, F. J., & Smith, D. K. (1999). A model function for the ocean-normalized  
377           radar cross section at 14 ghz derived from nscat observations. *Journal of Geo-*  
378           *physical Research: Oceans*, *104*(C5), 11499–11514.
- 379 Wright, C. W., Walsh, E., Vandemark, D., Krabill, W., Garcia, A., Houston, S., . . .  
380           Marks, F. (2001). Hurricane directional wave spectrum spatial variation in the  
381           open ocean. *Journal of Physical Oceanography*, *31*(8), 2472–2488.
- 382 Young, I. R. (1999). *Wind generated ocean waves*. Elsevier.
- 383 Young, I. R. (2006). Directional spectra of hurricane wind waves. *Journal of Geo-*  
384           *physical Research: Oceans*, *111*(C8).
- 385 Young, I. R. (2017). A review of parametric descriptions of tropical cyclone wind-  
386           wave generation. *Atmosphere*, *8*(10), 194.



Figure1.

Author Manuscript

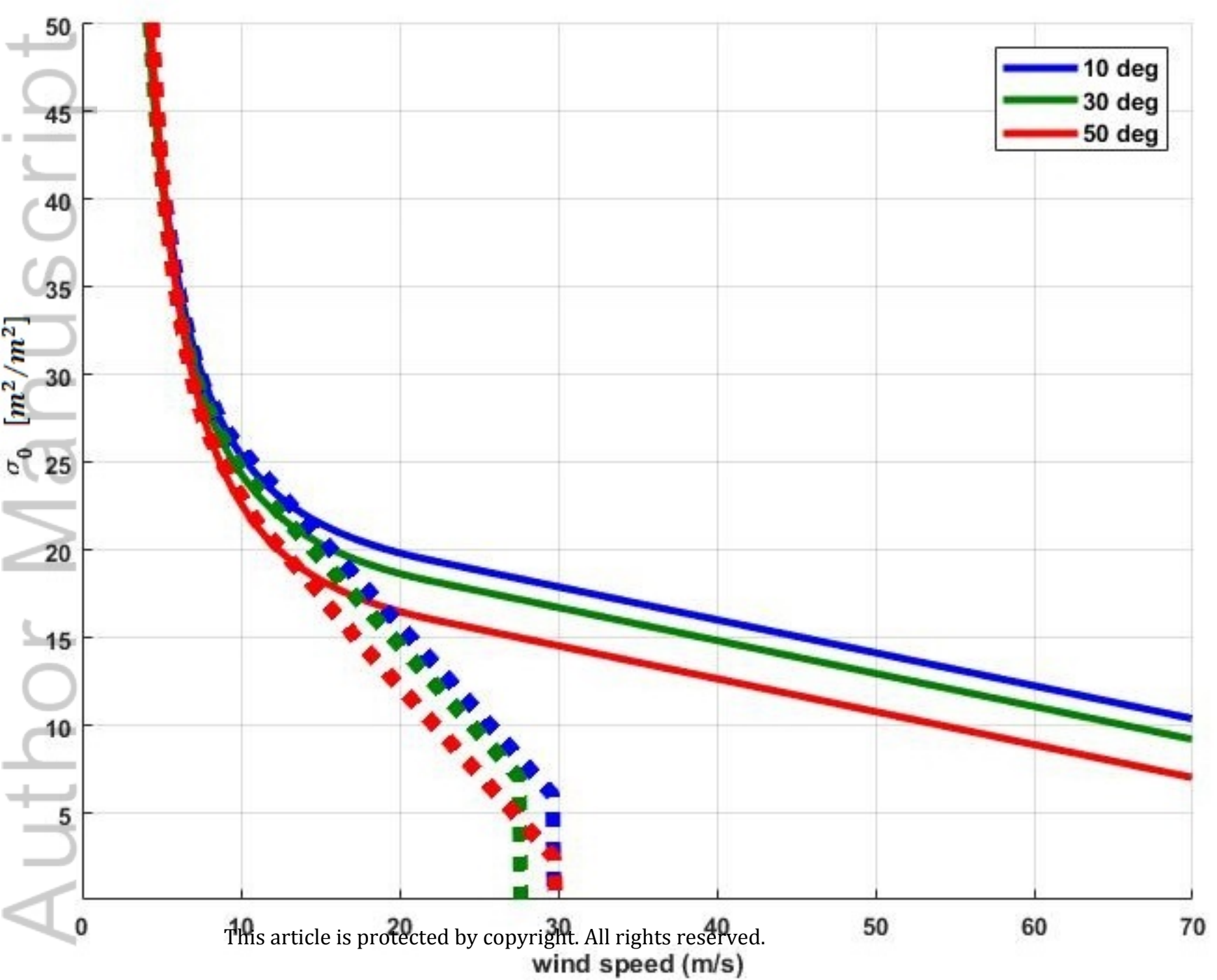


Figure 2.

Author Manuscript

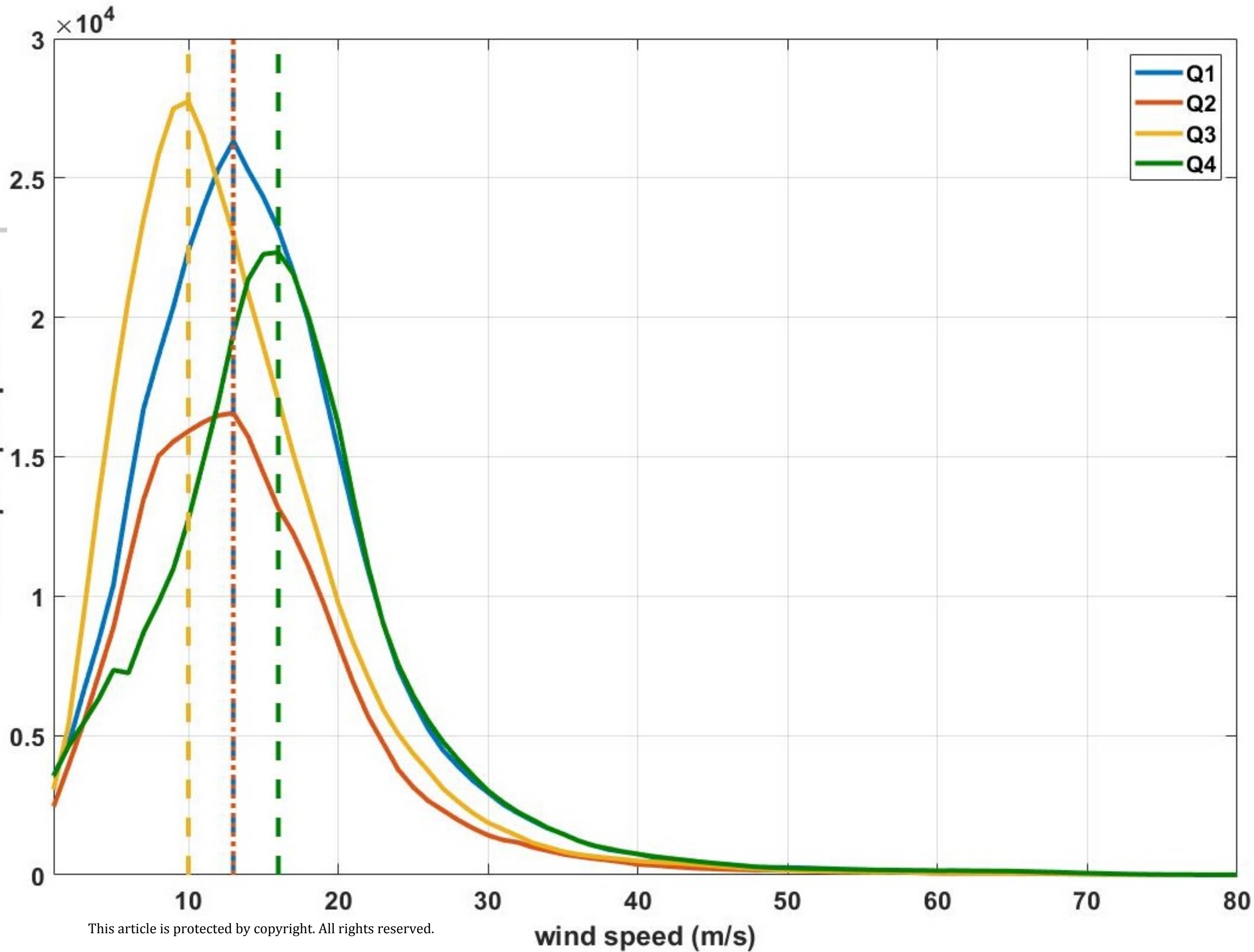


Figure 3 combined.

Author Manuscript

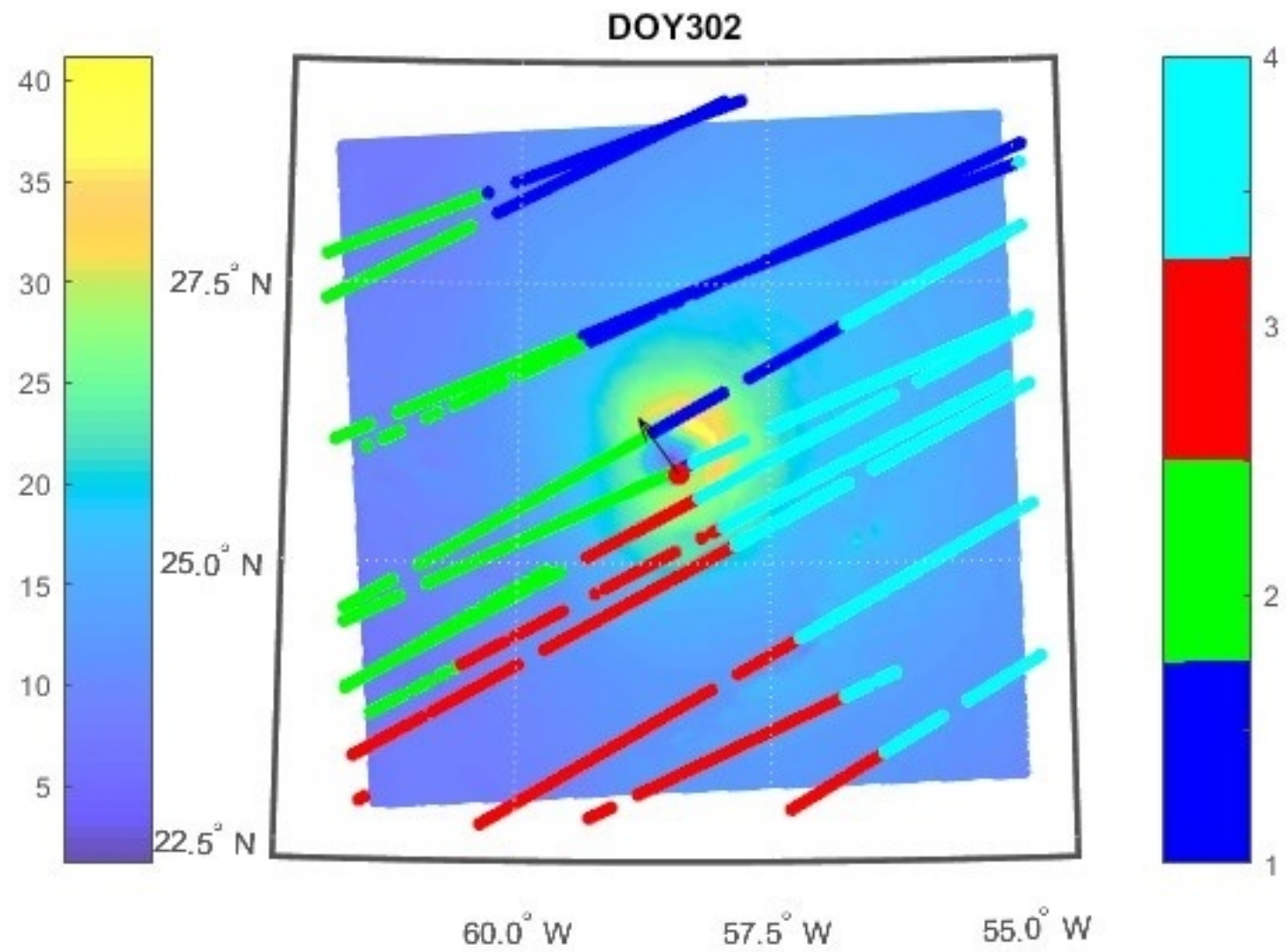
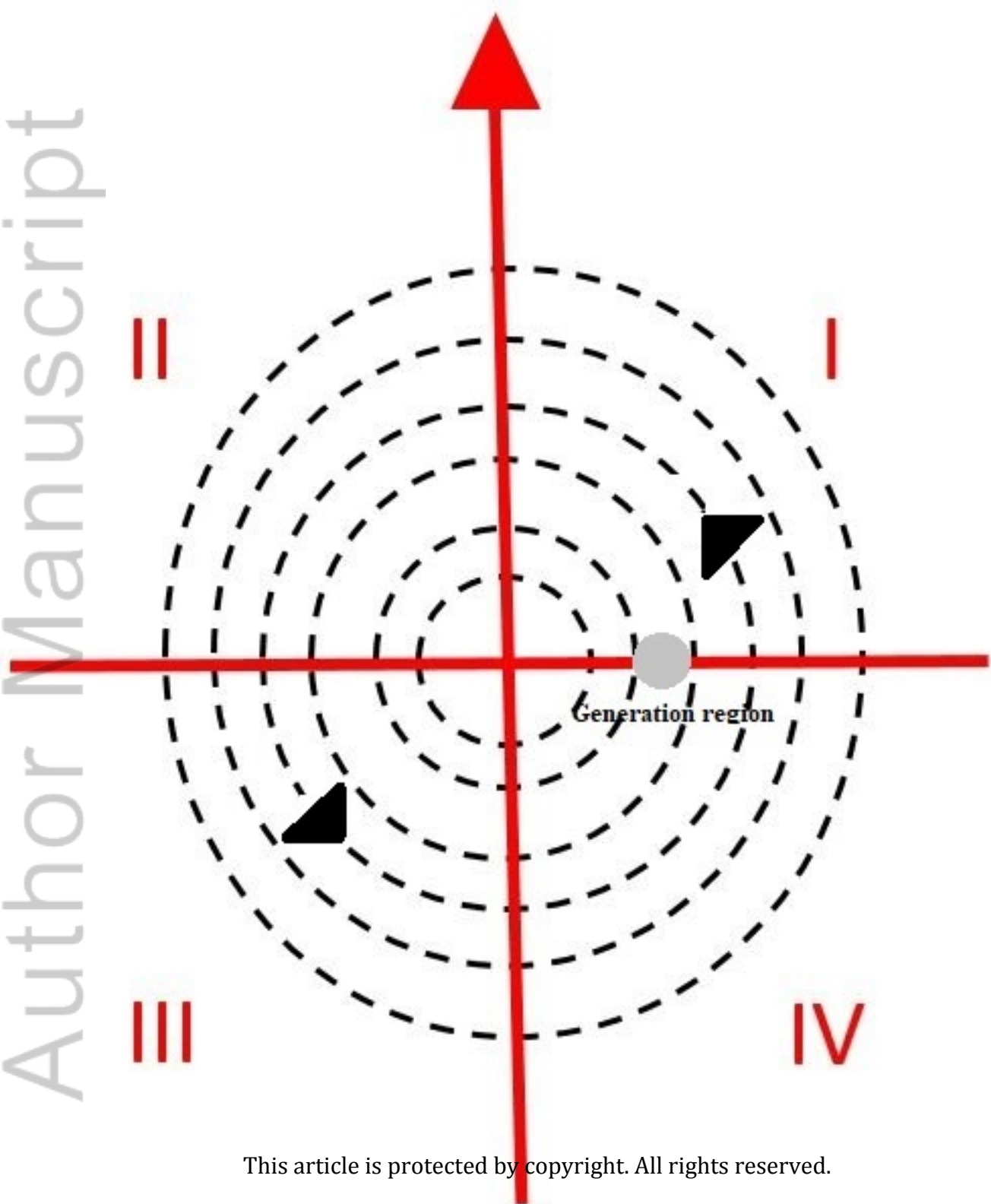




Figure 4 combined.

Author Manuscript

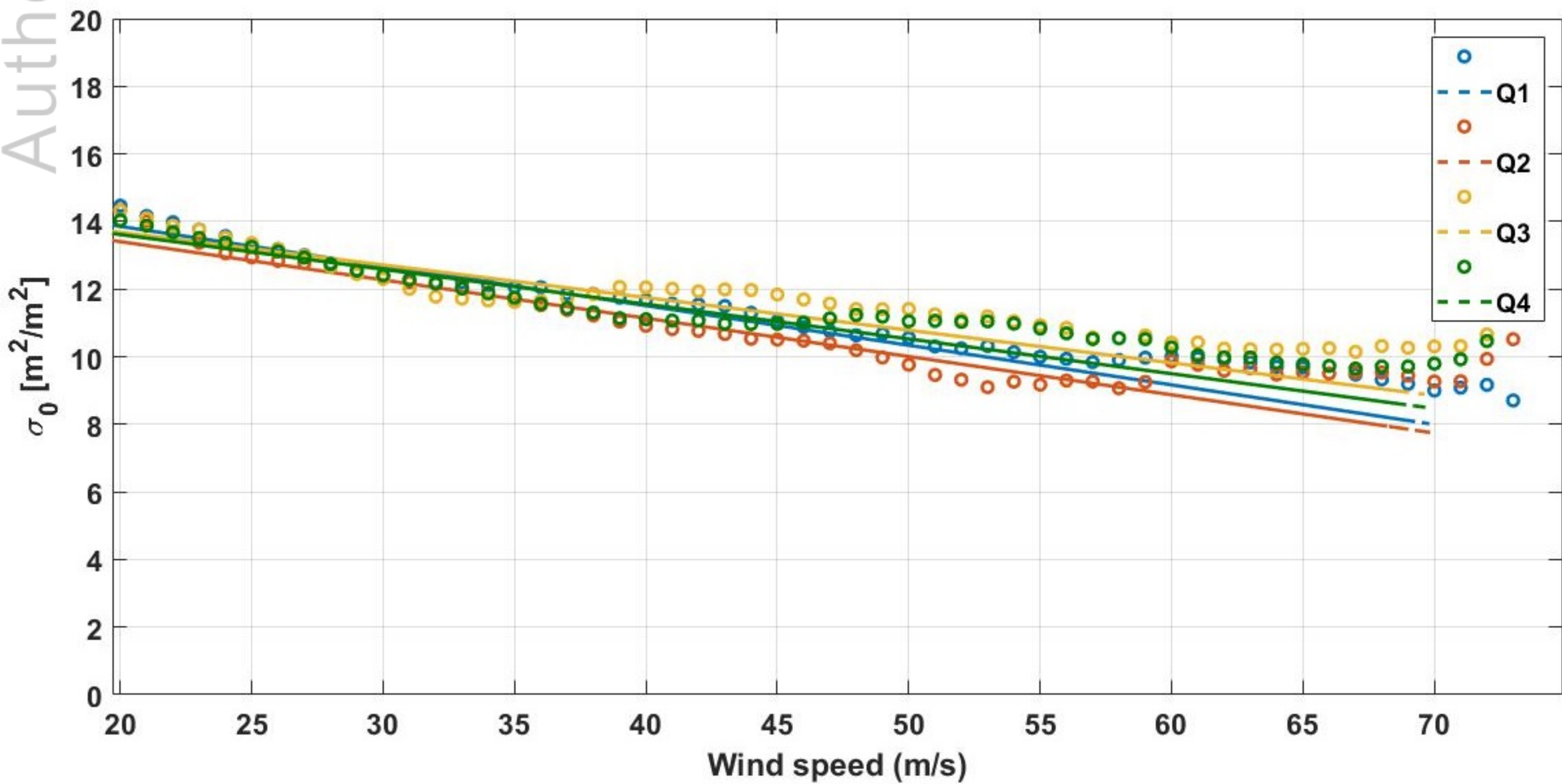
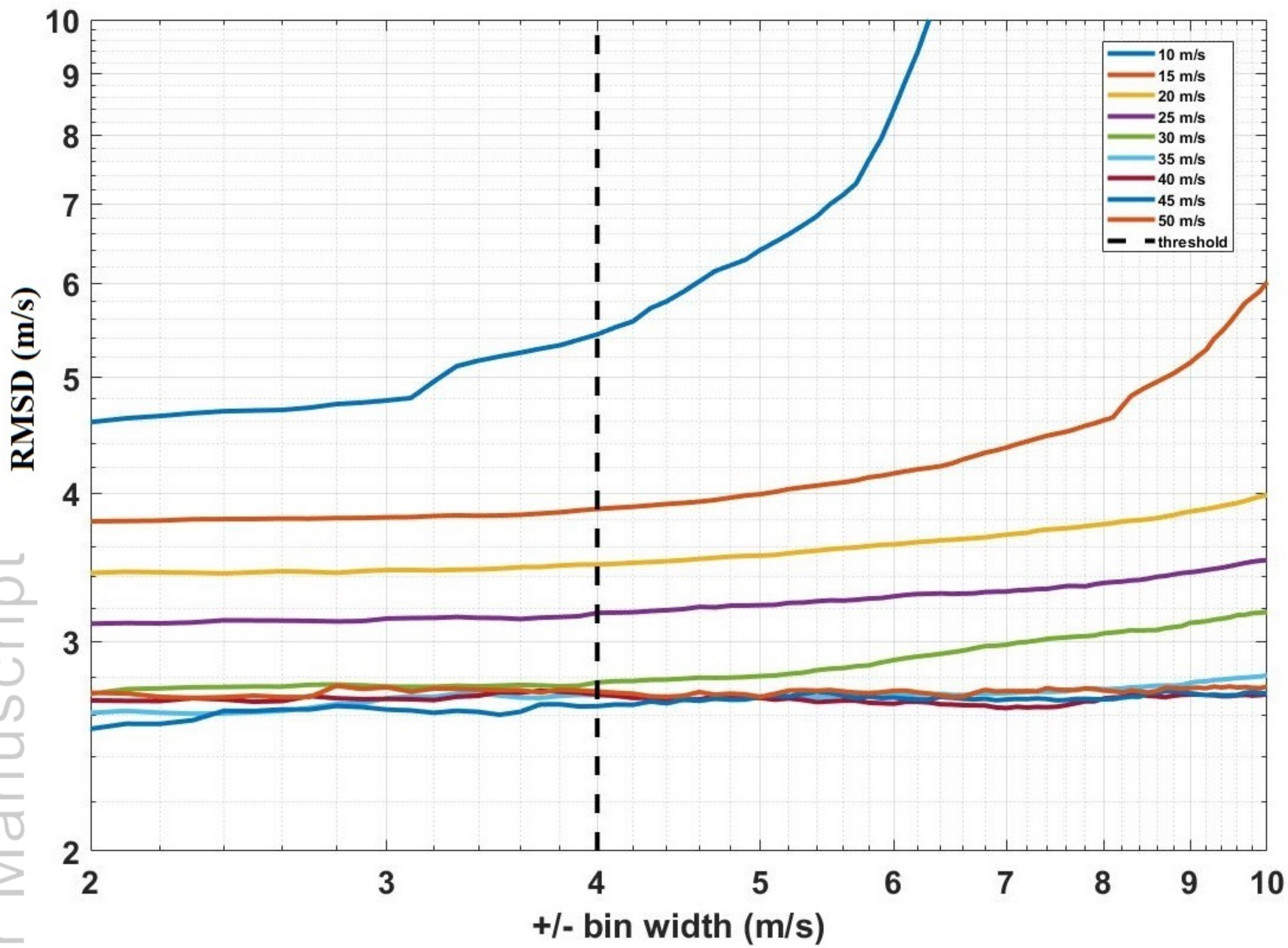


Figure 5 combined.

Author Manuscript



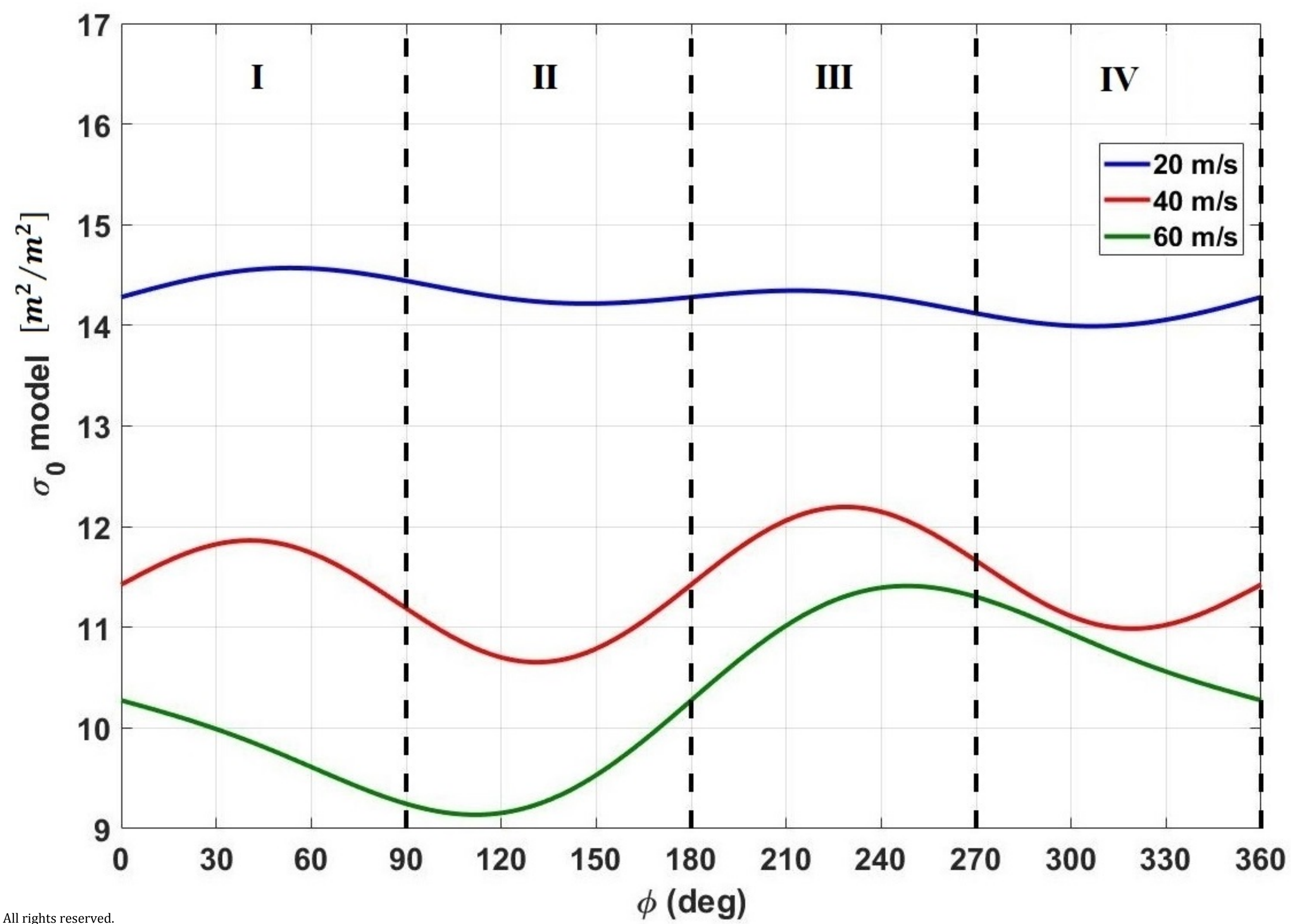
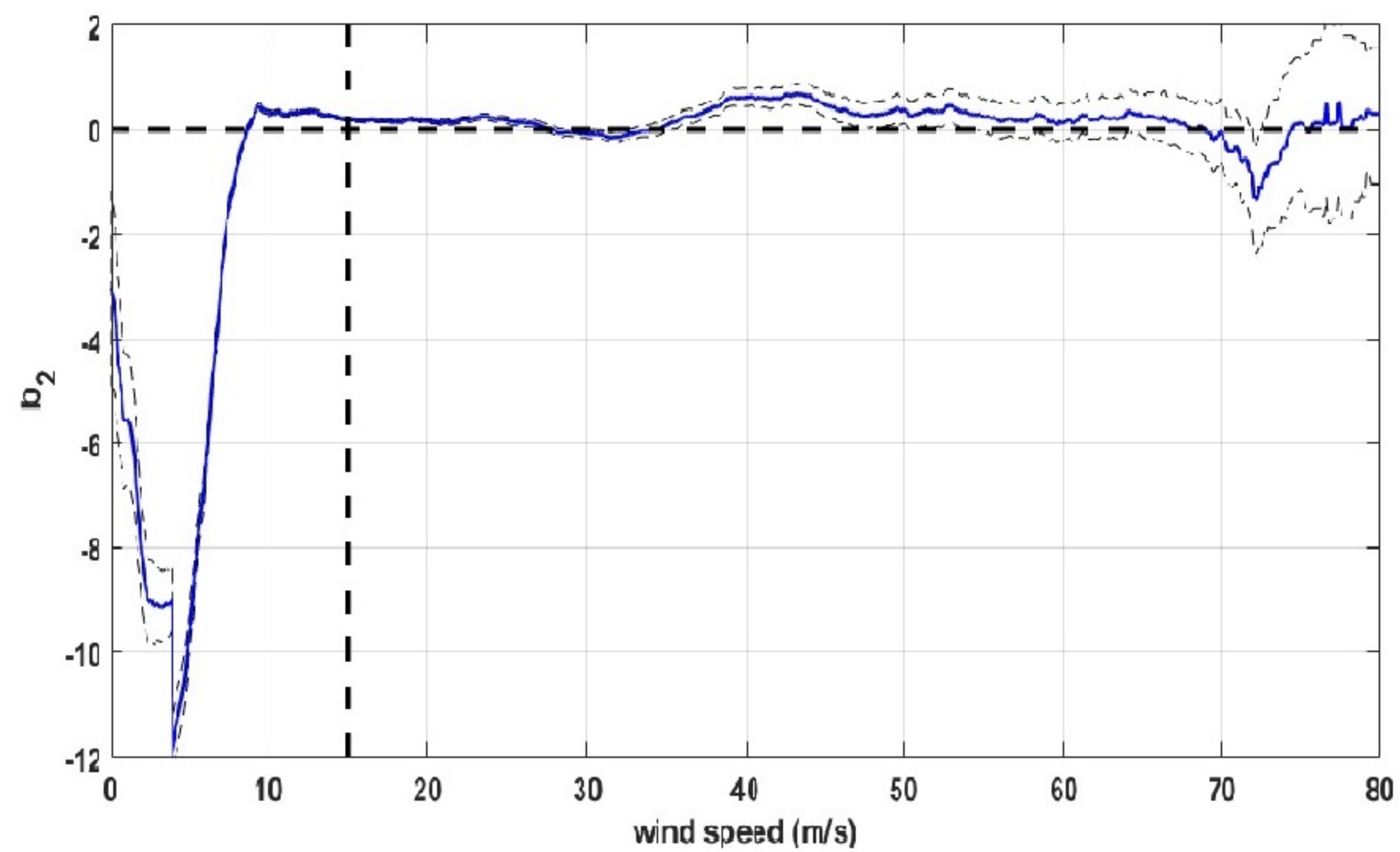
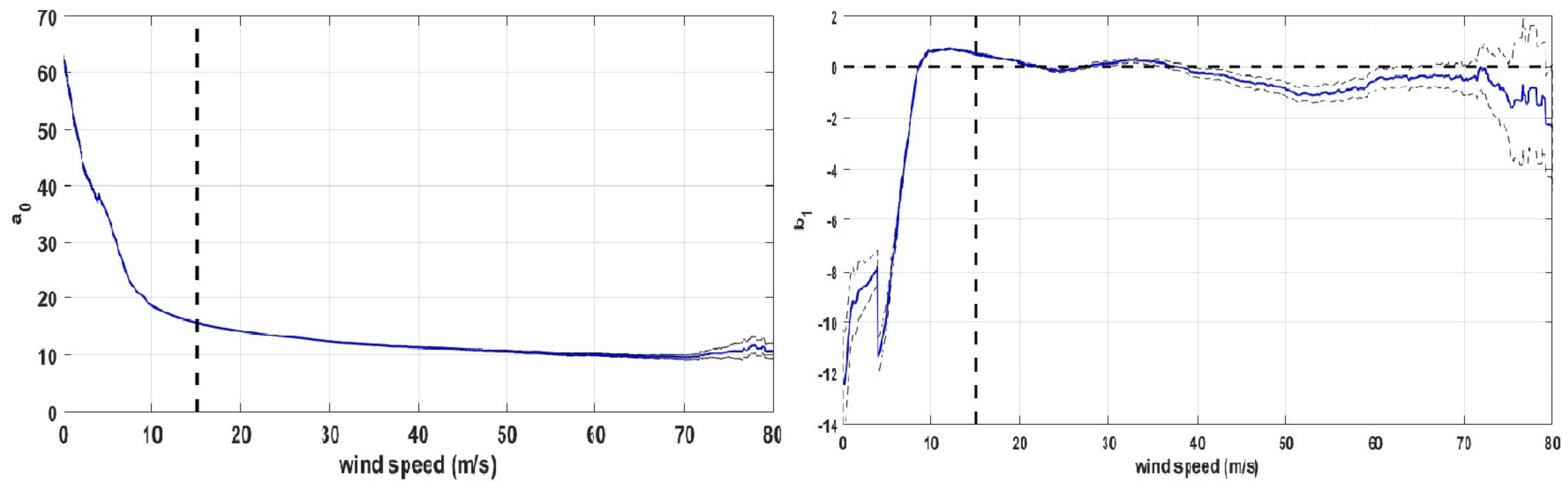


Figure 6.

Author Manuscript

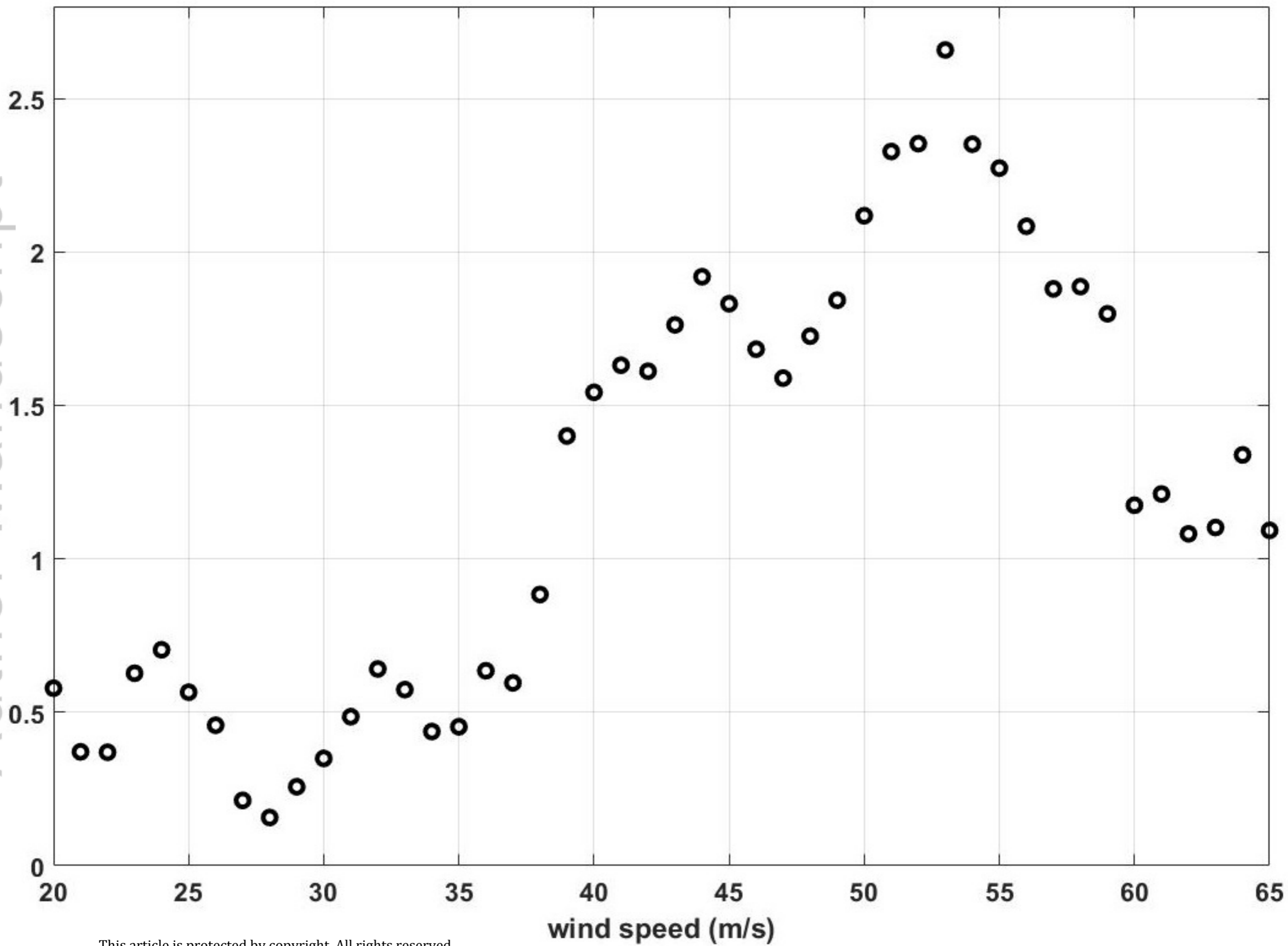




Figure 7 combined.

Author Manuscript

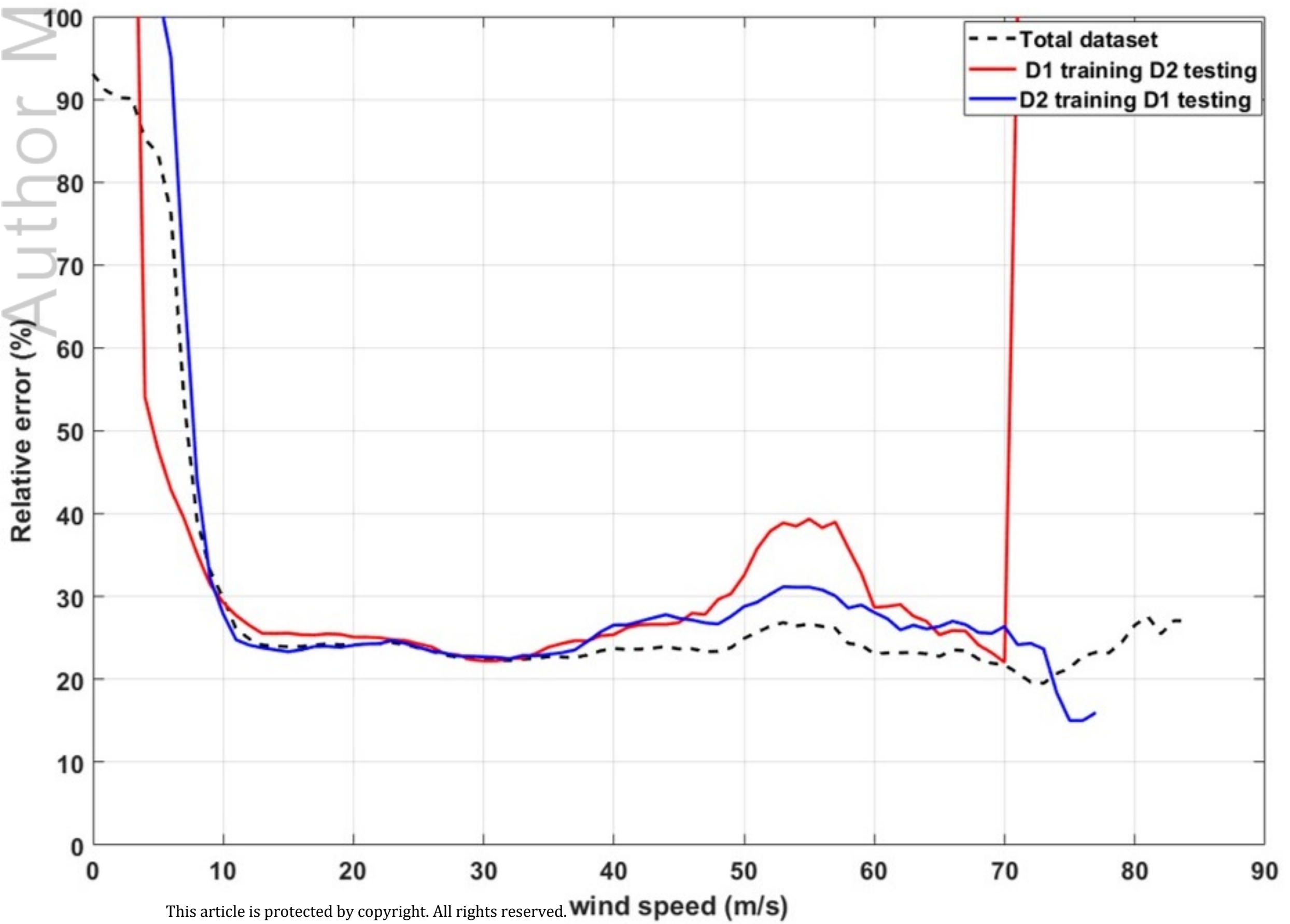
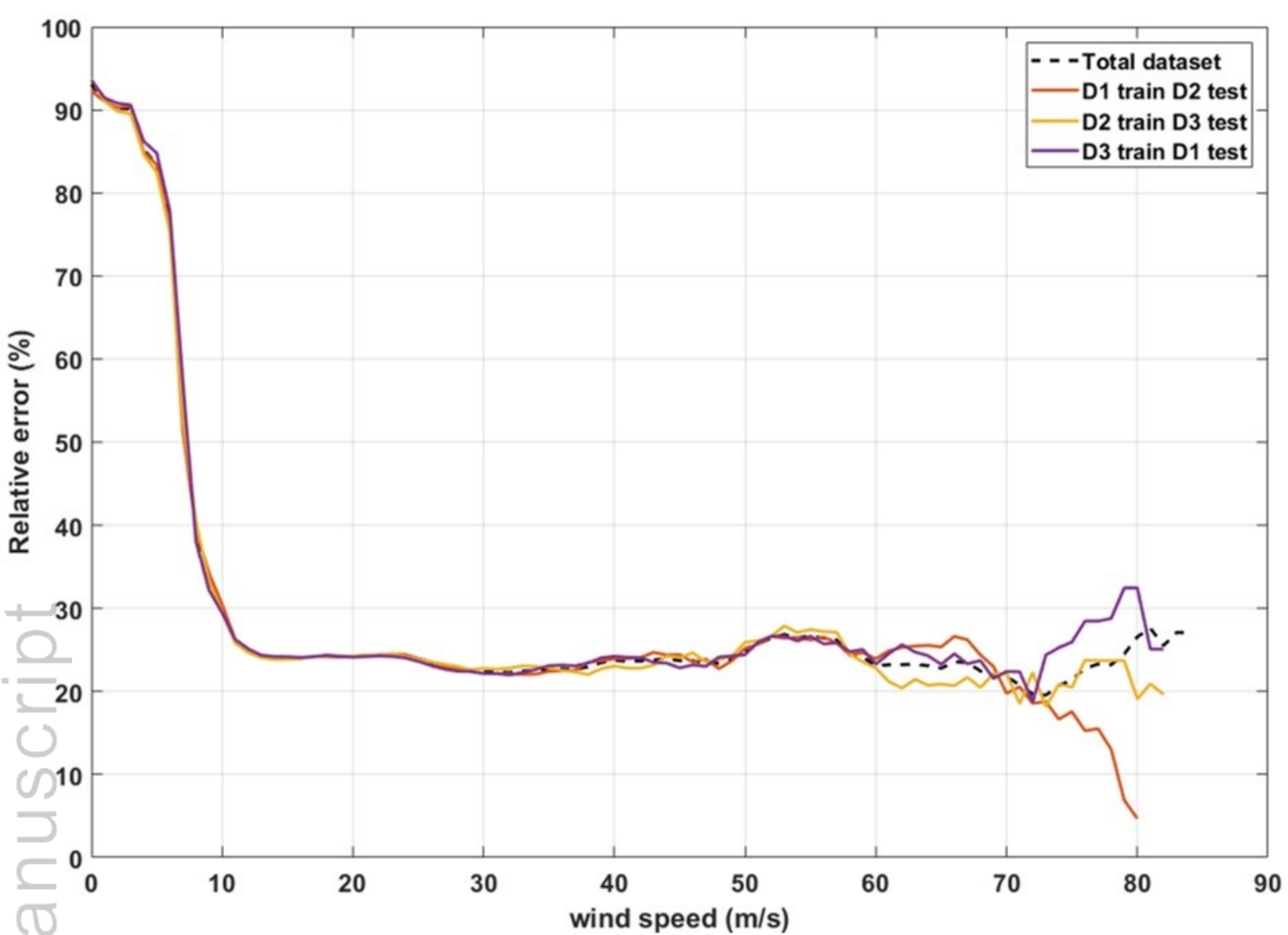


Figure 8.

Author Manuscript

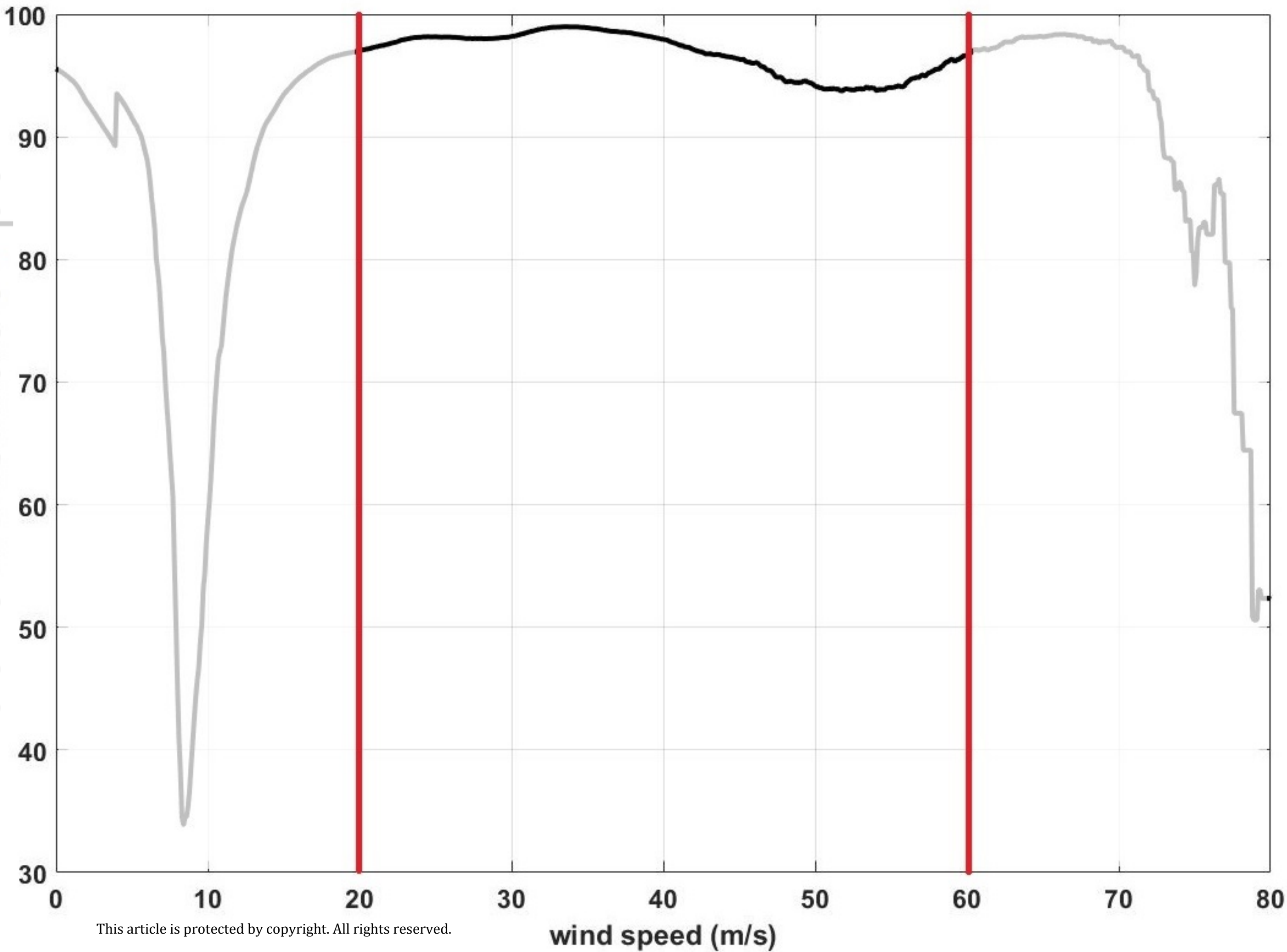


Figure 9.

Author Manuscript

